# Fabrication of electron's path based on carbonized polymer dots to accelerate photocatalytic hydrogen production kinetic for carbon nitride

Lei Ding [a], Ze-Nan Li [b], Ru-Yi Liu [a], Yan-Fei Li [a], Guo-Duo Yang [a], Zhen-Hui Kang [b,d,*], Bai Yang [c,**], Ming-Xiao Deng [a,**], Hai-Zhu Sun [a,**]

[a] National & Local United Engineering Laboratory for Power Batteries, College of Chemistry, Northeast Normal University, Changchun 130024, PR China
[b] Institute of Functional Nano & Soft Materials (FUNSOM), Jiangsu Key Laboratory for Carbon-Based Functional Materials & Devices, Soochow University, Suzhou 215123, PR China
[c] State Key Laboratory of Supramolecular Structure and Materials, College of Chemistry, Jilin University, Changchun 130012, PR China
[d] Macao Institute of Materials Science and Engineering, Macau University of Science and Technology, Taipa 999078, Macau Special Administrative Region of China

## A R T I C L E   I N F O

## A B S T R A C T

Constructing efficient path for electron mobility is significant for increasing carrier separation and transport ability but a great challenge. Herein, a unique shell based on carbonized polymer dots (CPDs) is fabricated to serve as electron's path for charge transfer from carbon nitrides (CN) to metal-based cocatalysts. This CPDs shell homogenously fixes each CPD on the catalyst surface through metal-N bonding, and possesses strong electron extraction ability by masterly controlling the pyridinic N structure. As a result, the obtained CN/MoP@CPDs-200 achieves an outstanding apparent quantum efficiency (9.4% at 450 nm), which is superior to CN/3 wt% Pt. Importantly, in-depth transient photo-induced voltage studies confirm the excellent charge extraction ability of CPDs shell, and thorough apparent kinetic analysis reveals that the photocatalytic hydrogen production process undergoes a Volmer-Heyrovsky mechanism that demonstrates the reduction reaction between photogenerated charges and water ($H^*+H_2O+e^- \rightarrow H_2\uparrow+OH^-$), which is a critical missing investigation in photocatalytic studies for CPDs.

## 1. Introduction

Hydrogen generation from photocatalytic water splitting is a promising and sustainable strategy to capture and convert solar energy into clean energy [1,2]. Since Wang et al. reported the application of carbon nitride (CN) in the field of photocatalytic hydrogen production in 2009, CN has become a star material due to its visible light response, easily tunable structure, low cost and good stability [3,4]. However, the limited active sites and rapid recombination of photogenerated carriers are the intrinsic shortcomings of CN, which prevents its practical application in photocatalysis [5–8]. To date, loading cocatalysts is an effective method to improve electrons and holes separation [9–12]. Unfortunately, the weak interfacial contact between cocatalysts and CN may lead to the accumulation or shedding of the cocatalysts on the CN surface in photocatalytic hydrogen generation process. Meanwhile, the

interface resistance always exists during the photocarriers transfer process under light irradiation, which abruptly reduces the separation efficiency of photocarriers [13–15]. Therefore, it is urgent and challenging to develop electron's path with low cost and high carriers transportation capacity between cocatalysts and CN [16].

Materials with high electrical conductivity have been reported for electron transport mediators, such as, noble metals, non-noble metals, graphene, and $Ni_2P$, etc [10,17,18]. For example, He et al. synthesized $CdS/Ni_2P/g-C_3N_4$ composite, in which $Ni_2P$ was used as electron mediators to improve charge separation and photocatalytic efficiency [19]. However, the interfacial transport resistance of the composite material still needs to be improved for this "electron-bridge" design strategy. In order to accelerate the charge transfer between the semiconductor and the cocatalyst, an ideal electron conductor, not only needs to be uniformly distributed on the surface of the cocatalyst, but also have a strong

interaction with the semiconductor and the cocatalyst [20,21]. Therefore, constructing a structure that interconnects the electron conductors is an effective solution but also a challenge.

Carbon dots (CDs), as an emerging 0D star carbon material, possess the merits of high electrical conductivity, good biocompatibility, high stability and low cost [22–24]. Therefore, CDs have been employed extensively as various roles in the field of photocatalysis, such as visible light sensitizer [25,26], electron transport layer [27,28] and hole transfer channel [29,30] and so on [31]. Meanwhile, the functional groups on their surfaces (e.g., -NH$_2$), allow them to form "metal-CDs" bonds with transition metal-based materials, facilitating photogenerated electron transfer [32]. For example, Xia et al. reported amine-functionalized graphene quantum dots (GQDs-NH$_2$) as a support material for single-atom catalysts. The small size of GQDs-NH$_2$ and the strong chelating effect between metal cations and amine groups endow the single-atom catalysts with high transition-metal-atom density and excellent electrocatalytic performance [33]. As an important member of CDs, carbonized polymer dots (CPDs) with graphitized carbon cores and polymer chains shells, have the advantage of easy composition and structure tunability [34]. Compared with other CDs such as GQDs, the tuning of hybrid atom will be much easier and more precisely [4]. As known, among different nitrogen dopant atoms (pyridinic, pyrrolic and graphitic N), pyridinic N has a basic lone pair of electrons localized to the aromatic system so that it exhibits a stronger basicity than pyrrolic N and graphitic N [35]. Hence, pyridinic N tends to accept electrons from adjacent C atoms, thereby facilitating charge transfer [36]. The content of pyridinic N can be easily controlled during the synthesis of CPDs. In addition, the more abundant groups on the surface of CPDs compared to other CDs make it possible to fabricate hierarchical structure via direct cross-linking or other chemical reactions [37,38]. Therefore, CPDs are ideal units for building conductive shells. However, few investigations report such kind of shell, let alone the in-depth photocatalytic mechanism.

In addition, it is well known that the electrocatalytic hydrogen evolution reaction (HER) is divided into two steps in an alkaline solution. Firstly, the H atoms resulting from the dissociation of water are adsorbed onto the electrocatalyst to form H*, also known as the Volmer reaction [39]. Subsequently, H* may undergo the Heyrovsky reaction (H*+H$_2$O+e$^-$→H$_2$↑+OH$^-$) or the Tafel reaction (2 H*→H$_2$↑) to form hydrogen [40,41]. However, for the photocatalytic HER process, many efforts have focused on studying the migration of photogenerated charges inside the catalyst [1,42,43]. The mechanism involved in the reduction reaction between photogenerated charges and water at the photocatalyst surface has rarely been investigated, which is critical to the study of photocatalytic process.

Herein, a structure controllable CPDs shell with homogeneous strong interactions with both photocatalyst and cocatalyst was fabricated as a bridge to transport photogenerated charges between the CN and cocatalysts, which effectively accelerates the extraction of photogenerated charges. Molybdenum phosphide (MoP) is chosen as a representative non-precious metal cocatalysts due to its Pt-like electronic structure, high electrical conductivity and high stability [44–46]. The formation of uniform Mo-N-C interaction reduces the interfacial transfer resistance and promotes the rapid migration of photogenerated carriers. The optimized sample CN/MoP@CPDs-200 exhibits an H$_2$ evolution rate of 1084 $\mu$mol g$^{-1}$h$^{-1}$, which is four times higher than that of CN/MoP, as well as the excellent apparent quantum efficiency (AQE) of 9.4% at 450 nm. The transient photo-induced voltage (TPV) tests demonstrate that CPDs shell accelerates the charge extraction from CN to MoP. Significantly, the surface reaction kinetics analysis reveals that the hydrogen evolution reaction (HER) on the CN/MoP@CPDs proceeds through the Volmer-Heyrovsky process in electrocatalysis.

## 2. Experimental details

### 2.1. Preparation of CN

Urea (10 g) was placed in a crucible with a lid and heated in a muffle furnace at a heating rate of 2.3 °C/min to 550 °C and maintained for 4 h. Then, the bulk carbon nitride, BCN, was obtained.

3 g of BCN was heated to 500 °C at 2 °C/min and kept for 2 h in an air atmosphere. After natural cooling of the sample, carbon nitride nanosheets were obtained, noted as CN.

### 2.2. Preparation of CPDs

6.3 g of citric acid (0.0328 mol) and 1.8 g of ethylenediamine (0.0292 mol) were dissolved into 60 mL of water and stirred for 30 min. The clarified solution obtained was transferred to a 100 mL Teflon-lined autoclave and heated at 200 °C for 5 h. After cooling naturally, the resulting brown solution was filtered through a syringe filter (0.22 $\mu$m) to eliminate impurities. Subsequently, the solution was transferred to a dialysis bag (molecular weight cut-off to 500 D) for two days of purification and the final product was freeze-dried for 48 h to obtain CPDs-200. The synthesis method of CPDs-160 and CPDs-240 was similar to that of CPDs-200, except that the heating temperature was changed to 160 °C and 240 °C, respectively.

### 2.3. Preparation of MoP@CPDs

750 mg of (NH$_4$)$_6$Mo$_7$O$_{24}$ and 200 mg of CPDs were dispersed in 30 mL of water and sonicated for 30 min. The solution was transferred to a 100 mL round bottom flask and heated at 80 °C for 12 h. The brown powder Mo-precursor@CPDs was obtained by freeze-drying.

0.1 g of Mo-precursor@CPDs and 0.5 g of NaH$_2$PO$_2$·2H$_2$O were ground in a mortar and then calcined at 500 °C for 1 h under N$_2$ atmosphere at a ramp rate of 5 °C/min and then ramped to 750 °C with a ramp rate of 2 °C/min for 2 h. The obtained MoP@CPDs were centrifuged for 3 times and dried in the oven at 60 °C for 12 h. Pure MoP nanoparticles were synthesized by directly heating 0.1 g (NH$_4$)$_6$Mo$_7$O$_{24}$ and 0.5 g of NaH$_2$PO$_2$·2H$_2$O at 750 °C for 2 h in the N$_2$ atmosphere with a heating rate of 2 °C/min.

### 2.4. Preparation of CN/MoP@CPDs

100 mg CN and 7 mg MoP@CPDs were dispersed into 10 mL ethanol and sonicated for 60 min. After natural evaporation to remove the ethanol, the product was annealed at 300 °C for 2 h in order to reinforce the interaction between CN and MoP@CPDs. The synthesis method of CN/MoP is similar to that of CN/MoP@CPDs, except that the MoP@CPDs is changed to MoP.

## 3. Results and discussion

Scheme 1 shows the synthesis procedure of CN/MoP@CPDs. Firstly, the composition controllable CPDs with high conductivity core and functional surface groups are prepared. Then, the CPDs shell is formed on the surface of MoP through crosslinking, phosphorylation and annealing reactions. The homogenous distribution of CPDs on the surface of MoP is realized to ensure a strong and uniform interaction between MoP and CN nanosheets via the chelating effect between Mo ions and surface functional groups of CPDs while a smooth electron transport path is generated at inner of the CPDs shell. The composition of this CPDs shell is manipulated by tuning the carbonization temperature in order to further improve the electron transport ability.

### 3.1. Regulation of CPDs Structure

The CPDs morphology with different compositions was investigated
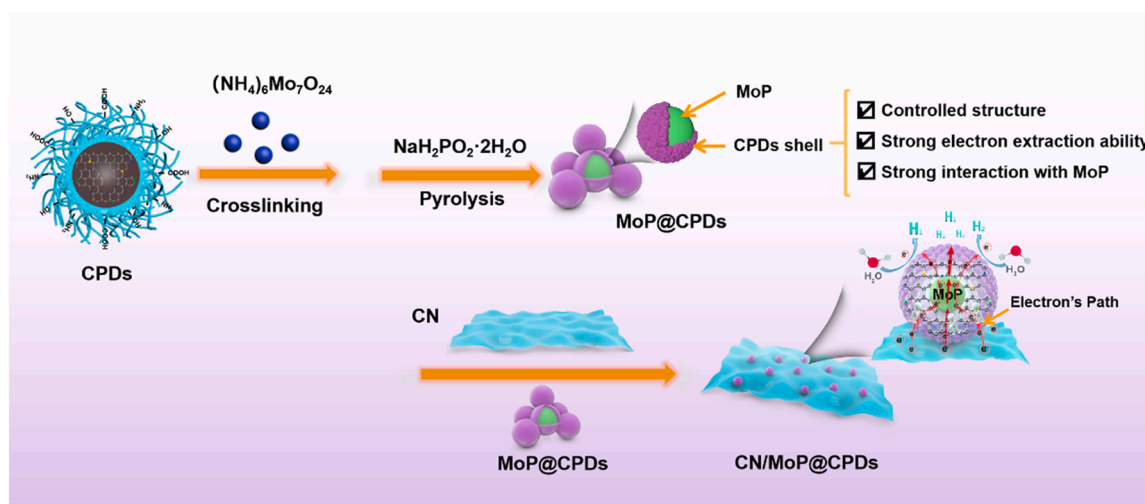
**Scheme 1.** The synthesis procedure of CN/MoP@CPDs.

by transmission electron microscopy (TEM), as shown in Fig. 1a and Fig. S1. From Fig. 1a, the TEM images of CPDs-200 display narrow distribution with average size of approximately 2.95 nm. The interplanar spacing of 0.21 nm is correlated with the (100) planes of graphite carbon [47]. Fourier transform infrared (FT-IR) spectra of the three CPDs are depicted in Fig. 1b. The signals at ~3429 cm$^{-1}$, ~3253 cm$^{-1}$, ~2942 cm$^{-1}$, ~1700 cm$^{-1}$, ~1652 cm$^{-1}$, ~1566 cm$^{-1}$, ~1169 cm$^{-1}$ and ~1045 cm$^{-1}$ are attributed to -OH, -NH$_2$, C-H, C=O, C=N, C-C, C-O-C and C-O stretching in all three CPDs, indicating that the three

CPDs contain similar surface functional groups [48]. As shown in Fig. S2, both CPDs-200 and CPDs-240 exhibit a broad peak at about 22° and 26° in X-ray powder diffraction (XRD) patterns, respectively, corresponding to (002) planes of carbon [49].

Five peaks approximately at ~284.2, ~284.7, ~285.2, ~286.1, and ~287.9 eV are observed in the X-ray photoelectron spectroscopy (XPS) high resolution C 1s spectra of three CPDs (Fig. S3), corresponding to C-C/C=C, C-N, C-O/C-OH, C=N, and C=O, respectively. The specific composition of N in different CPDs was proved by XPS high resolution N
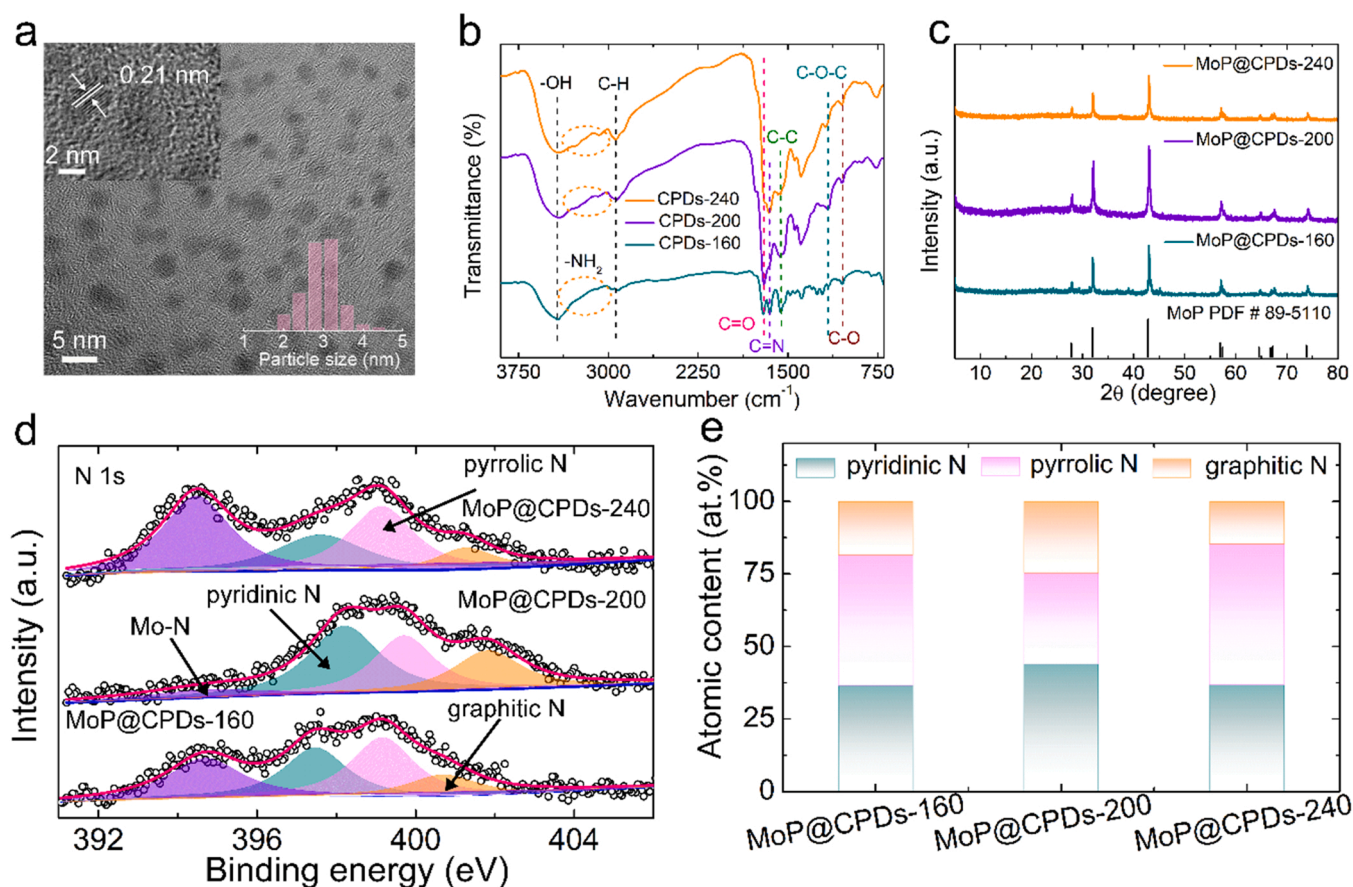


**Fig. 1.** (a) TEM images of CPDs-200; (b) FT-IR spectra of CPDs; (c) XRD patterns; (d) XPS high resolution N 1s spectra; (e) Distribution of different N functionalities in MoP@CPDs-160, MoP@CPDs-200 and MoP@CPDs-240, indicating that MoP@CPDs-200 contains the highest proportion of pyridinic N.

1s spectra (Fig. S4). For all CPDs, the N 1s spectra are divided into four N species, including pyridinic N (~399.4 eV), -NH$_2$ (~400.0 eV), pyrrolic N (~400.5 eV) and graphitic N (~401.2 eV) [48].

Fig. S5 illustrates the distribution of the different N species for pure CPDs. As reported in the literature, CPDs-160 are mainly polymer clusters due to the lower carbonization temperature [50]. As temperature increases, graphitized carbon cores gradually appear and grow with nitrogen doping concentration reaching about 27%. At such concentration, the formation energy of pyridinic N is lower than that of pyrrolic N and graphitic N, so that the CPDs-200 contains higher proportion of -NH$_2$ and pyridinic N [51]. When the carbonization temperature further increases to 240 °C, the carbon cores grow bigger, accompanied by the possible transformation of some pyridinic N into graphitic N, as well as the decrease of surface functional group content. As a result, the proportion of pyridinic N and -NH$_2$ decreases and that of graphitic N increases in CPDs-240. Therefore, the CPDs-200 contains the highest proportion of -NH$_2$ and pyridinic N in three CPDs, which is advantageous for coordination with metal ions and the enhancement of photocatalytic activity.

### 3.2. Construction of CPDs shell

CPDs shell was constructed on the MoP surface by freeze-drying and high-temperature phosphorylation processes using CPDs as building block. The XRD cuspidal peaks (27.9°, 32.2°, 43.1°, 57.5°, 64.9°, 67.9° and 74.3°) are discovered in the MoP@CPDs samples, respectively, which ascribe to the (001), (100), (101), (110), (111), (102) and (201) planes of hexagonal MoP (JCPDS 89-5110) (Fig. 1c). As shown in FT-IR spectra (Fig. S6), the surface of MoP@CPDs samples possesses abundant functional groups, such as C-O and N-H, which is conducive to further contact with CN [52]. As shown in Fig. S7, the C 1s spectrum is fitted to C-C/C=C and C≡N/C-N. Fig. 1d displays the XPS pattern of N 1s, in which the peaks located at ~401.8, ~399.7 and ~398.2 eV are attributed to the graphitic N, pyrrolic N and pyridinic N [35]. Notably, new characteristic peaks appear near ~394.7 eV for the Mo-N bond, indicating a strong chemical interaction between MoP and CPDs. Furthermore, semi-quantitative analysis of XPS N 1s spectra shows that the MoP@CPDs-200 sample still contains the highest content pyridinic N atoms among the three MoP@CPDs samples (Fig. 1e), which is favorable for electron transfer due to the strong electronegativity of pyridinic N atoms [35].

The structure of CPDs shell was confirmed by SEM (Fig. S8) and TEM. The high-resolution TEM (HRTEM) image in Fig. 2a, b and Fig. S9 clearly shows that the CPDs are homogenously distributed in the shell, and hence provide uniform interaction with MoP, leading to the successful coating on MoP. Meanwhile, the lattice spacing of 0.28 nm
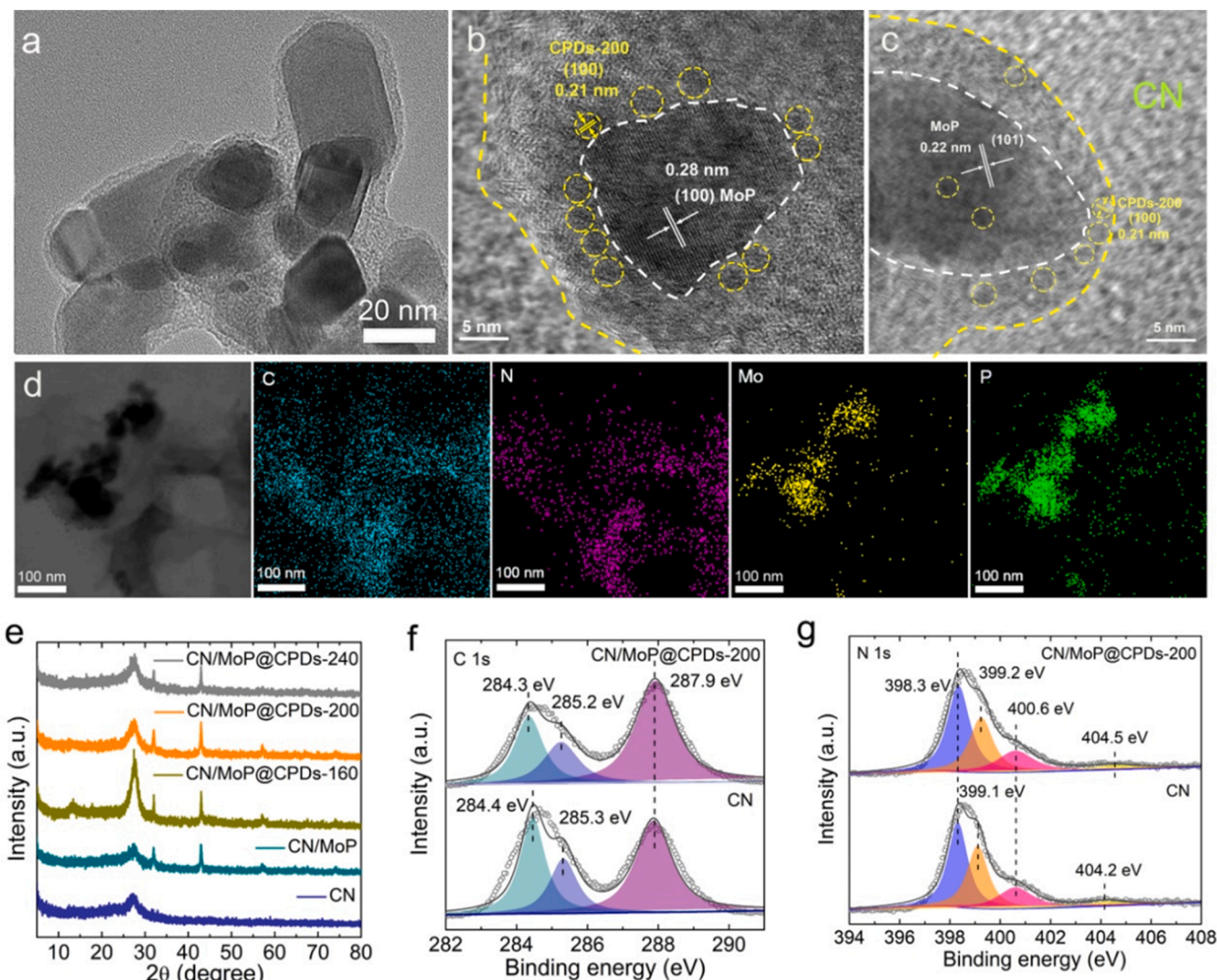


**Fig. 2.** (a, b) TEM and HRTEM images of MoP@CPDs-200; (c) HRTEM images of CN/MoP@CPDs-200; (d) HAADF-STEM image of CN/MoP@CPDs-200 and its corresponding element mapping images of C, N, Mo, P; (e) XRD patterns; XPS spectra of (f) C 1s, (g) N 1s in CN and CN/MoP@CPDs-200.

corresponds to the (100) lattice plane of MoP. After assembling MoP@CPDs nanoparticles with CN, the MoP@CPDs-200 are still uniformly distributed on the CN surface (Fig. S10). The HRTEM image in Fig. S11 and Fig. 2c clearly show that the CPDs shell is embedded between CN and MoP, forming an electron path between MoP and CN. This preparation method accurately places the "electron-bridge" between the two photocatalysts, effectively avoiding the uneven contact of the ternary catalyst. Elemental mapping shows that C, N, Mo and P elements in CN/MoP@CPDs-200 nanosheets are homogeneously spread on CN nanosheets (Fig. 2d).

As depicted in Fig. 2e, the pristine CN displays two diffraction peaks at 13.3° and 27.4° attributed to the (100) and (002) crystal planes of carbon nitride, respectively [53]. Moreover, the composites exhibit diffraction peaks of MoP, indicating the successful preparation of CN/MoP and CN/MoP@CPDs photocatalysts. As depicted in Fig. S12, the FT-IR spectrum for CN exhibits broad peaks at 3000–3500 cm$^{-1}$, deriving from the N-H stretching vibrations [54]. The peaks located from 1000 to 1800 cm$^{-1}$ represent the stretching vibrations mode of C-N heteroring framework. The absorption peak around at 810 cm$^{-1}$ corresponds to the tri-triazine ring units [55,56]. For CN/MoP and

CN/MoP@CPDs, no obvious difference is discovered in the FT-IR spectra, suggesting that neither the MoP nor the MoP@CPDs will change the microstructure of CN.

As observed in Fig. 2 f, there are three peaks at 284.4 eV, 285.3 eV and 287.9 eV in the C 1s spectrum of pristine CN, corresponding to C-C, C-(N)$_3$, and N = C-N bonds, respectively [57,58]. However, compared to the pure CN, the peaks for C-C and C-(N)$_3$ of CN/MoP@CPDs-200 shift to the lower binding energy, while another peak is unchanged. A similar shift is discovered in the N 1s spectra of CN and CN/MoP@CPDs-200. As depicted in Fig. 2 g, four feature peaks are detected on the N 1s spectrum of the CN which are attributed to C-N = C groups (398.3 eV), N-(C)$_3$ groups (399.1 eV), H-N-C groups (400.6 eV), and π-excitation (404.2 eV) [59]. Impressively, both N-(C)$_3$ groups and π-excitation peaks display positive shift in the N 1s spectrum of CN/MoP@CPDs-200. It is well known that the binding energy is negatively related to the surface electron density. Therefore, the simultaneous shift of the C 1s and N 1s peaks in opposite directions indicates a strong chemical bonding interaction between CN and MoP@CPDs [60]. The Mo 3d spectrum of CN/MoP@CPDs-200 is displayed in Fig. S13. The peaks centered at 227.0 eV and 230.9 eV are derived from Mo 3d$_{5/2}$ and 3d$_{3/2}$
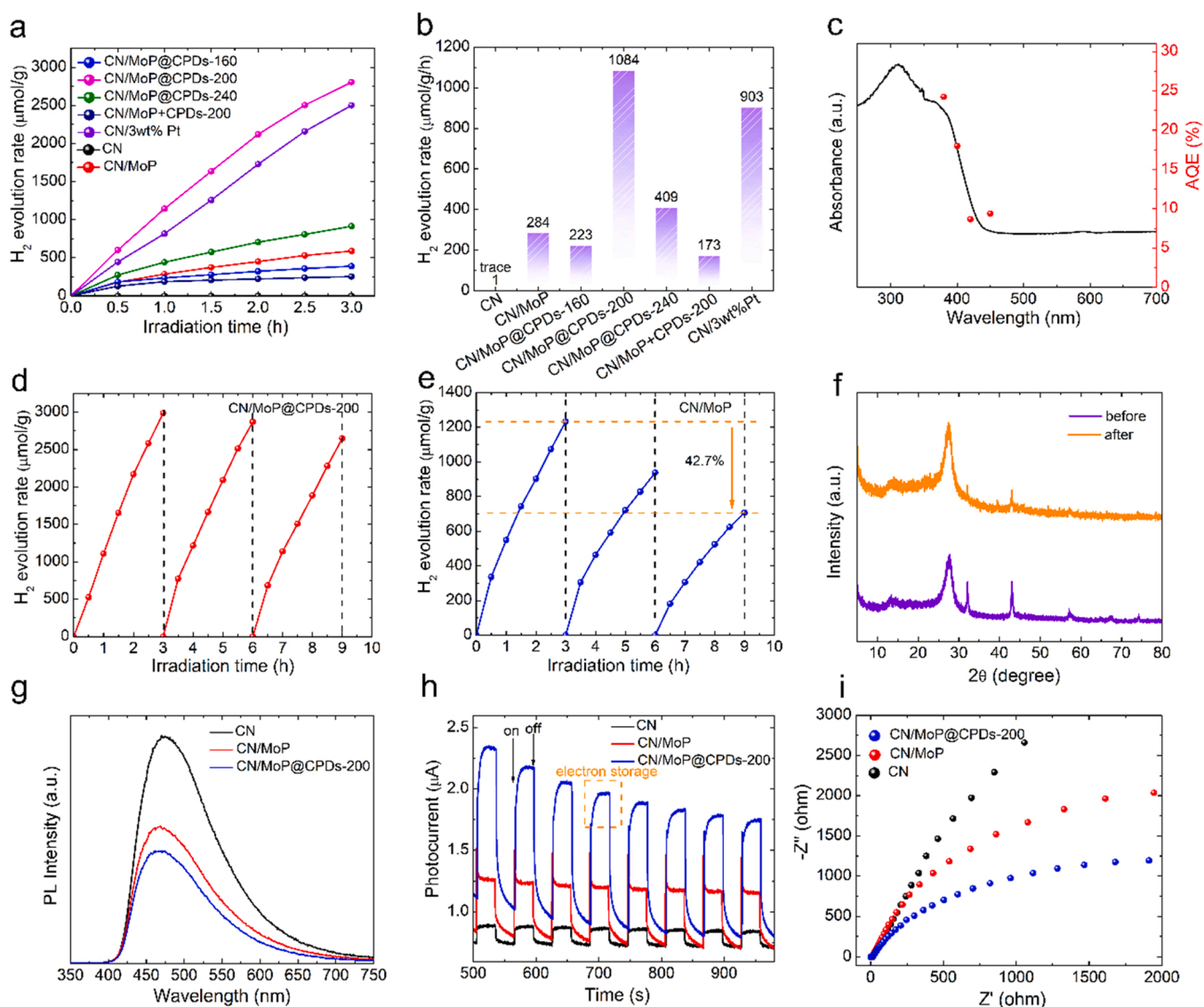


**Fig. 3.** (a, b) Photocatalytic H$_2$ evolution rates over various samples under visible light irradiation (λ > 420 nm); (c) Wavelength-dependent AQE for CN/MoP@CPDs-200 at different wavelength; (d, e) Recycle runs of H$_2$ evolution over the CN/MoP@CPDs-200 and CN/MoP; (f) XRD of CN/MoP@CPDs-200 before and after cycling tests; (g) PL spectra; (h) Transient photocurrent responses (i–t curves) under visible-light irradiation (>420 nm); (i) EIS spectra in the dark.

in MoP. Moreover, the peaks located at 232.3 eV and 235.3 eV are ascribed to the Mo $3d_{5/2}$ and $3d_{3/2}$ in $MoO_x$, originating from the surface oxidation of MoP. Specially, a peak at 227.8 eV is detected in Mo 3d spectrum, corresponding to the Mo-N bond in CN/MoP@CPDs-200 [9]. In addition, from Fig. S14, the P 2p peaks at 128.3 eV and 132.8 eV are observed, which indexed to the Mo-P bond and $P_2O_5$ species, respectively [44]. These results confirm the strong interactions between CN, CPDs shell and MoP, which becomes a new electron transfer channel.

### 3.3. Photocatalytic activities

From Fig. 3a and b, during the photocatalytic $H_2$ evolution, trace amounts of $H_2$ are produced from pure phase CN due to rapid carrier recombination. The average hydrogen evolution rate of CN/MoP is 284 μmol $g^{-1}h^{-1}$, indicating that MoP as a cocatalyst promoted the separation and transfer of carriers. Specially, CN/MoP@CPDs-200 exhibits an impressive hydrogen evolution rate of 1084 μmol $g^{-1}h^{-1}$, increased by nearly 4-fold from the CN/MoP, suggesting that the CPDs shell can effectively reduce the interface transfer resistance. The nitrogen adsorption-desorption data further confirm the superiority of CN/MoP@CPDs-200 (Fig. S15 and S16). Compared to CN (65.42 m$^2$ g$^{-1}$) and CN/MoP (61.01 m$^2$ g$^{-1}$), CN/MoP@CPDs-200 possesses a larger BET surface area of 86.20 m$^2$ g$^{-1}$, which provides more active sites and facilitates mass transfer.

In addition, the influence of CPDs shell composition on the activity of CN/MoP@CPDs was further explored. As shown in Figs. 3a and 3b, the $H_2$ evolution rates of CN/MoP@CPDs-160 and CN/MoP@CPDs-240 are 223 and 409 μmol $g^{-1}h^{-1}$. The slight decrease in the performance of CN/MoP@CPDs-160 compared to CN/MoP may attribute to the diffusion limitation of protons. The enhancement of the photocatalytic activity is mainly related to the increase of pyridinic N atoms content. CPDs with pyridinic N atoms content of ~43.9 at% (CPDs-200) has the strongest transfer ability for the interfacial electron separation of CN/MoP. Moreover, CN/MoP+CPDs-200 prepared by mixed annealing method only exhibit a relatively low photocatalytic hydrogen production rate of 173 μmol $g^{-1}h^{-1}$, probably because the pure CPDs covering some reactive sites of CN/MoP, further suggesting its essential to precisely embed CPDs between CN and MoP. Meantime, CN/MoP@GQDs samples were prepared by the same method as CN/MoP@CPDs-200 except that CPDs-200 were replaced with GQDs. As shown in Fig. S17, the superior photocatalytic activity of CN/MoP@ CPDs-200 further indicates that the N-doped structure of CPDs-200 is able to extract more photogenerated electrons to participate in the reduction reaction. Additionally, the performance of CN/MoP@CPDs-200 is even higher than that of CN/3 wt % Pt (903 μmol $g^{-1}h^{-1}$), suggesting that MoP@CPDs-200 has promising application in photocatalytic hydrogen production (Fig. 3b).

From Fig. 3c, the AQE of CN/MoP@CPDs-200 are calculated to be 24.2%, 18.0%, 8.7% and 9.4% at λ = 380, 400, 420 and 450 nm, respectively, which exceeds many other reported CN-based photocatalysts (Table S2). As illustrate in Figs. S18-S20, the wavelength range of CN/MoP is extended compared with bulk CN, which probably is ascribed to the intense light harvesting ability of MoP. Meanwhile, the CN/MoP@CPDs-200 sample further displays a slightly red-shift absorption edge due to the strong light absorbance capacity of CPDs, which facilitates the emergence of photogenerated charge carriers. The AQE plots matches well with the optical absorbance of CN/MoP@CPDs-200, demonstrating the photocatalytic $H_2$ generation reaction is photoexcitation driven.

Besides, to evaluate the stability of the photocatalysts, CN/MoP and CN/MoP@CPDs-200 were used to employ a cyclic $H_2$ evolution experiment. As shown in Figs. 3d and 3e, no significant decrease in the hydrogen production activity of the CN/MoP@CPDs-200 is observed while the hydrogen production activity of CN/MoP decreased by 42.7% after the continuous photocatalytic cycling reaction (9 h). This indicates that the strong and homogeneous interaction brought by CPDs shell not only accelerates the charge transfer but also endows CN/MoP@CPDs-

200 with superior durability. Furthermore, no apparent changes are observed in their crystal structure and morphology, which further indicates the stability of CN/MoP@CPDs-200 (Fig. 3f and Fig. S21).

### 3.4. Photocatalytic mechanism

#### 3.4.1. Photoelectrochemical properties

To illustrate the charge transfer process between the CN and MoP@CPDs-200, Mott-Schottky plots were conducted to estimate the Fermi energy level potential ($E_F$) and conduction band (CB) edge potential. As depicted in Fig. S22, the flat band potential ($E_{fb}$) of CN and MoP@CPDs-200 is determined to be - 1.53 and - 1.22 V vs. NHE ($E_{NHE}$ = $E_{Ag/AgCl}$ + 0.197 V), respectively [61]. In addition, positive slopes are noted for the Mott-Schottky plots of CN and MoP@CPDs-200, indicating that they are n-type semiconductors [62,63]. Generally, $E_{fb}$ reflects the $E_F$ of the semiconductor and is typically 0–0.2 V more positive than the CB of an n-type semiconductor [47,64]. Therefore, the CB of CN is approximated as $-$ 1.73 V vs. NHE and the valence band potential (VB) of CN is calculated as 1.65 V vs. NHE according to the UV-Vis absorption spectra (Fig. S19). Based on the above analysis, the relative band structures of CN and MoP@CPDs-200 is depicted in Fig. S23a. When CN is composited with MoP@CPDs-200, the electrons in CN will migrate towards MoP@CPDs-200 until the $E_F$ reaches equilibrium due to the higher $E_F$ of CN than MoP@CPDs-200. At the same time, CB and VB of CN bend upward, and Schottky barrier will be formed [65,66]. Under visible light irradiation, the photogenerated electrons on the CB of CN will be transferred to the MoP@CPDs-200 surface for the reduction reaction, while the holes retained on the VB of CN are consumed by the sacrificial agent (TEOA) (Fig. S23b). In this case, CPDs-200 with strong electron extraction capability will help more photogenerated electrons to migrate to the catalyst surface, thus enhancing the photocatalytic performance.

Fig. 3g illustrates the PL spectra of CN, CN/MoP and CN/MoP@CPDs-200. Compared to CN, the lower intensity CN/MoP is attributed to the establishment of a Schottky barrier that promotes carrier separation. Notably, the CN/MoP@CPDs-200 sample demonstrates the lowest PL peak intensity, which signifies that the CPDs shell further facilitates carrier separation due to the high conductivity brought by pyridinic N atoms [65,67]. Electrochemical experiments were employed to investigate the charge separation efficiency of the photocatalysts. Fig. 3h displays the photocurrent responses of CN, CN/MoP and CN/MoP@CPDs-200. Compared with CN and CN/MoP, CN/MoP@CPDs-200 shows the strongest photocurrent response signal, indicating that CPDs shell is favorable for the rapid separation of light-generated charges. More importantly, the charge storage properties are also shown in Fig. 3h (orange frame), which is consistent with the results of TPV tests [68]. Next, Nyquist plots were used to evaluate the charge transfer resistance of the photocatalyst. From Fig. 3i, CN/MoP@CPDs-200 shows the smallest semicircle radius, indicating the fastest interfacial electron transfer rate [65,69–71].

As shown in Fig. 4a, the TPV tests of different samples were carried out to study the interfacial charge transfer kinetics. According to Fig. 4b, the $t_{max}$ values of CN/MoP@CPDs-200 ($t_{max4}$=2.7200 ms) and CN ($t_{max1}$=2.7040 ms) are shorter than CN/MoP ($t_{max2}$=2.8013 ms), illustrating that CN/MoP@CPDs-200 and CN have fast charge extraction rates. As is depicted in Fig. 4c, the shaded area (A) represents the maximum number of charges extracted from the samples, which are 0.0411, 0.0231 and 0.0297 for CN, CN/MoP and CN/MoP@CPDs-200, respectively [72]. In addition, attenuation constant (τ) was used to estimate the rate of the charge recombination process of the photocatalysts (Fig. 4d) [73]. Although the maximum charge extraction of CN/MoP is smaller than that of CN, it has a longer value of τ ($τ_2$ = 0.4688 ms) than CN ($τ_1$ = 0.1623 ms), indicating that the formation of heterojunctions slows down the charge recombination process. Significantly, $τ_4$ of CN/MoP@CPDs-200 (0.5707 ms) is remarkably longer than that of CN/MoP, strongly demonstrating that the charge recombination of
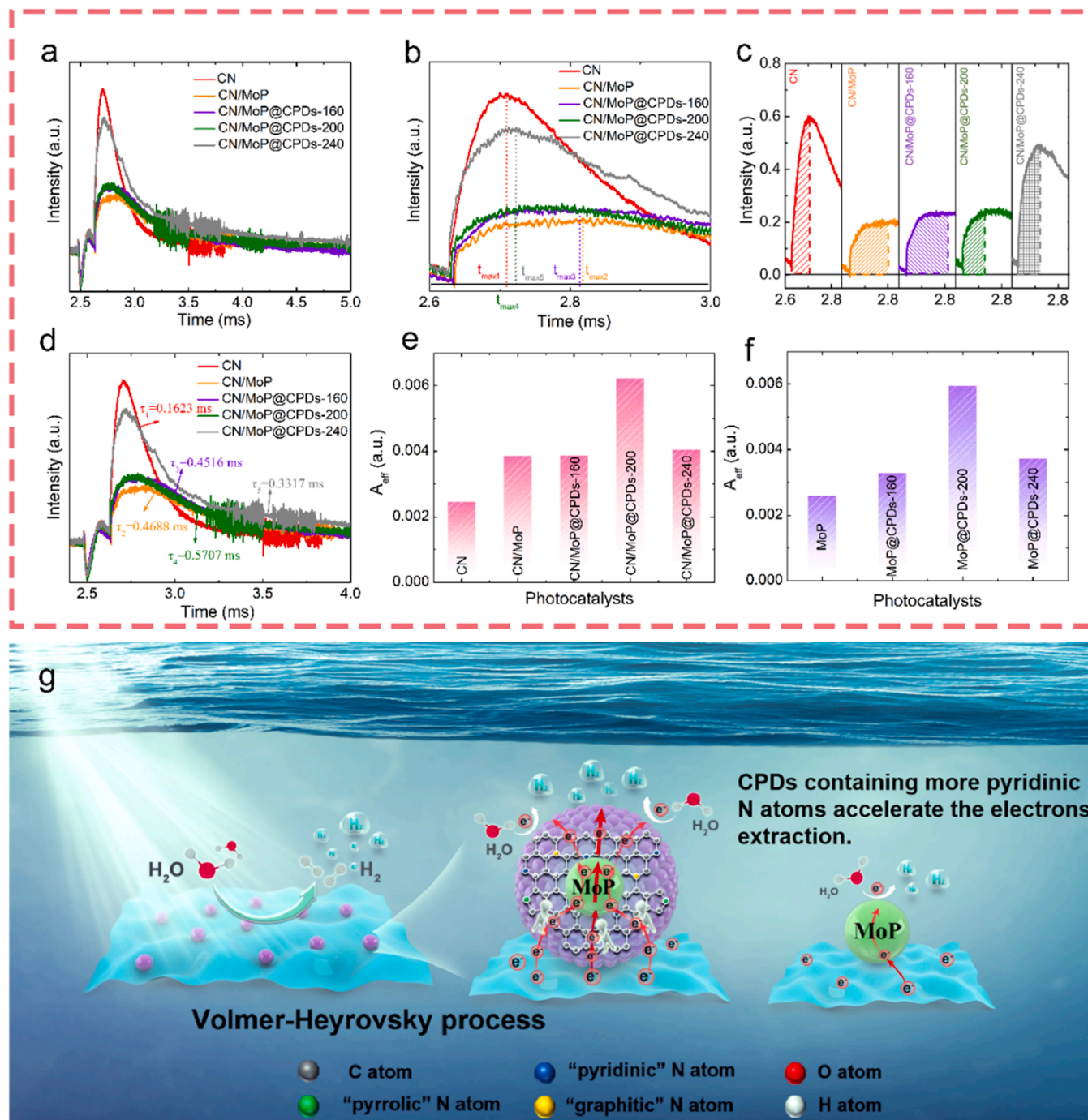
**Fig. 4.** (a) TPV curves; (b) Maximum charge extraction time; (c) Charge extraction; (d) Charge attenuation time; (e, f) Comparison of $A_{eff}$; (g) The photocatalytic mechanism diagram.

CN/MoP@CPDs-200 is inhibited upon the introduction of CPDs shell, due to the charge storage properties of CPDs. The effective electron concentration is calculated from the equation $A·\tau/t_{max}$, representing the number of charges that ultimately participate in the photocatalytic reaction. As shown in Fig. 4e, CN/MoP@CPDs-200 has the highest effective electron concentration, which means that the electron sink effect of CPDs limits the charge recombination, and thus more electrons are extracted to participate in the photocatalytic reaction.

To further investigate the effect of CPDs shell composition on charge extraction, TPV tests of MoP, MoP@CPDs-160, MoP@CPDs-200 and MoP@CPDs-240 were performed and the relevant data are listed in Table S1 and Fig. 4f. Fig. 4f shows a significant increase in the effective

surface charge from MoP (0.0026), MoP@CPDs-160 (0.0033), MoP@CPDs-240 (0.0037) to MoP@CPDs-200 (0.0060). This result indicates that CPDs shell containing more pyridinic N atoms accelerate the charge extraction, which facilitates the electron transfer from CN to MoP. In addition, the slightly increased content of graphitic N in MoP@CPDs-200 may also help to transport charge due to its high electrical conductivity [74].

According to the above structural analysis and performance tests, it can be inferred that the synergistic effect of MoP and pyridinic N may be the main factor in enhancing the photocatalytic hydrogen production performance of CN/MoP@CPDs-200. In order to determine the active sites of the CN/MoP@CPDs-200 composites, phosphate acid ($H_3PO_4$)

was used to block the pyridinic N sites according to a previously reported method [35]. As demonstrated in Fig. S24a, the overpotential increases with the increasing concentration of $H_3PO_4$ at current densities of 10 and 60 mA cm$^{-2}$, suggesting a decrease in HER activity. The changes in the content of surface species before and after $H_3PO_4$ soaking were further investigated by XPS. From Fig. S24c and d, XPS spectra of N 1s show that the ratio of pyridinic N species decreases with increasing $H_3PO_4$ concentration. Therefore, the pyridinic N is considered as one of the active sites [75]. Furthermly, KSCN solution was used as poisoning agent for metal-centered active sites [76]. As shown in Fig. S24a, the electrode treated with the KSCN solution shows a high overpotential, indicating that the metal species also work as active sites [77].

To elucidate the effect of the active sites on the electrochemical kinetics of HER, we fitted the Tafel slope based on the Linear sweep voltammetry (LSV) curves. As shown in Fig. S24b, the Tafel slope of pure MoP@CPDs-200 (0 M $H_3PO_4$) is 71 mV dec$^{-1}$. After treatment with $H_3PO_4$ and KSCN solutions, samples exhibit higher Tafel slope, indicating slower HER kinetics [46]. These comprehensive results suggest that the remarkable photocatalytic hydrogen production activity of CN/MoP@CPDs-200 results from the synergistic effect of MoP with pyridinic N [78].
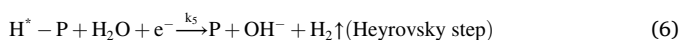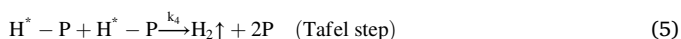
### 3.4.2. Apparent kinetics discussion

To gain a better insight into the charge extraction and reaction process, the apparent kinetic analysis of $H_2$ evolution on CN/MoP@CPDs is discussed. In our system, under visible light irradiation, the photogenerated electrons ($e_0$) are excited from VB of CN to CB, and the photogenerated holes ($h_0$) are retained on VB. Due to the excellent electron capture ability of MoP@CPDs, $e_0$ on the CB of CN are directly captured by MoP@CPDs ($e_1$) to participate in the HER process, while the $h_0$ are simultaneously eliminated by the sacrificial agent (TEOA). Therefore, the processes that $e_0$ and $h_0$ undergo can be expressed as the following equations.

$$e_0 + h_0 \xrightarrow{k_0} *_0 \tag{1}$$

$$e_0 + E1 \xrightarrow{k_1} e_1 \tag{2}$$

$$e_1 + h_0 \xrightarrow{k_2} *_1 \tag{3}$$

Here, $*_0$ is the exciton generated by the electron/hole recombination. E1 is the cocatalyst, referring to MoP@CPDs in this system, and $*_1$ is the exciton annihilated upon $e_1$ and $h_0$ recombination.

In alkaline solutions, the HER process includes two possible processes, Volmer-Tafel process or Volmer-Heyrovsky process, as shown in the following equations [79,80]:

$$H_2O + e^- + P \xrightarrow{k_3} H^* - P + OH^- \text{ (Volmer step)} \tag{4}$$

$$H^* - P + H^* - P \xrightarrow{k_4} H_2\uparrow + 2P \quad \text{(Tafel step)} \tag{5}$$

$$H^* - P + H_2O + e^- \xrightarrow{k_5} P + OH^- + H_2\uparrow \text{(Heyrovsky step)} \tag{6}$$

Here, P is photocatalysts. According to Eqs. (5) and (6), the relationship between the apparent rate of the HER ($\nu_{H_2}$) and the electron concentration ($c_e$) and proton concentration ($c_{H^+}$) can be expressed as the Eqs. (7) and (8).

$$\nu_{H_2} = k_4 \cdot c_{H^+}^2 \cdot c_e^2 \tag{7}$$

$$\nu_{H_2} = k_5 \cdot c_{H^+} \cdot c_e \tag{8}$$

According to the above TPV discussion, the number of effective electrons actually involved in the photocatalytic HER on the photocatalyst surface is correlated with the value of $A_{eff}$. Thus Eqs. (7) and (8) can be expressed as:

$$\nu_{H_2} = k_6 \cdot c_{H^+}^2 \cdot A_{eff}^2 \tag{9}$$

$$\nu_{H_2} = k_7 \cdot c_{H^+} \cdot A_{eff} \tag{10}$$

In the photocatalytic process, we assume that the proton concentration remains constant. As shown in Figs. 4a and 4b, the $\nu_{H_2}$ of CN/MoP@CPDs-160, CN/MoP@CPDs-240 and CN/MoP@CPDs-200 are 223 μmol g$^{-1}$h$^{-1}$, 409 μmol g$^{-1}$h$^{-1}$ and 1084 μmol g$^{-1}$h$^{-1}$, respectively. The corresponding $A_{eff}$ are 0.0037, 0.0041 and 0.0062. The $\nu_{H_2}$ increases linearly with increasing $A_{eff}$, indicating that the different CPDs shell will not affect the photocatalytic activities of the photocatalytic centers and the photocatalytic performance is not limited by the proton conduction in the presence of TEOA. Therefore, on the surface of the catalyst, photocatalytic hydrogen production mainly undergoes electrocatalysis based Volmer-Heyrovsky mechanism to achieve hydrogen reduction from protons. To confirm the electrochemical kinetics of HER, the Tafel slope was fitted according to the LSV curves. As illustrated in Fig. S25a and b, the Tafel slope of CN/MoP@CPDs samples were all greater than 120 mV dec$^{-1}$ in saturated $Na_2SO_4$ solution, indicating that the Volmer reaction is the rate-limiting step of the HER process [81]. To simulate the photocatalytic HER process in the presence of TEOA, the LSV test was carried out in 0.5 M $H_2SO_4$ solution (Fig. S25c and d). The Tafel slope of CN/MoP@CPDs-200 is 108 mV dec$^{-1}$, which is smaller than that of CN/MoP@CPDs-160 (116 mV dec$^{-1}$) and CN/MoP@CPDs-240 (117 mV dec$^{-1}$), indicating that the HER occurs via a Volmer-Heyrovsky process [46,82]. This result is in consistent with our speculation and confirms the faster HER occurred on CN/MoP@CPDs-200 sample.

## 4. Conclusions

In this work, a novel kind of CPDs shell is constructed as an electron transport path between semiconductor and cocatalysts. The homogenous distribution of CPDs in the shell ensures a uniform and strong interaction among cocatalysts, CPDs and photocatalysts, donating a stable structure and properties as well as high electron exaction. The control of pyridinic N structure in CPDs shell further improves the electron transport ability. As a result, the obtained CN/MoP@CPDs-200 achieves an impressive hydrogen evolution rate of 1084 μmol g$^{-1}$h$^{-1}$ with AQE of 9.4% at 450 nm, which is 4-fold as high as that of CN/MoP. Specifically, this performance for CN/MoP@CPDs-200 is even higher than CN/3 wt% Pt (903 μmol g$^{-1}$h$^{-1}$), demonstrating the enormous application potential in the photocatalytic HER. Moreover, the profound apparent kinetic investigation shows that the photocatalytic HER process undergoes a Volmer-Heyrovsky mechanism. The concept and the new CPDs shell as novel charge transport channels will provide more inspiration for the development of new composite catalysts applied in the field of photocatalysis.

## CRediT authorship contribution statement

**Lei Ding:** Investigation, Data curation, Software, Writing – original draft. **Ze-Nan Li:** Data curation, Writing – review & editing. **Ru-Yi Liu:** Investigation, Writing – review & editing. **Yan-Fei Li:** Writing – review & editing. **Guo-Duo Yang:** Software. **Zhen-Hui Kang:** Formal analysis, Data curation, Writing – review & editing. **Bai Yang:** Visualization, Writing – review & editing. **Ming-Xiao Deng:** Writing – review & editing. **Hai-Zhu Sun:** Conceptualization, Funding acquisition, Validation, Visualization, Writing – review & editing.

## Declaration of Competing Interest

The authors declare that they have no known competing financial interests or personal relationships that could have appeared to influence the work reported in this paper.

## Data availability

Data will be made available on request.

## Acknowledgements

## Appendix A. Supporting information

Supplementary data associated with this article can be found in the online version at doi:10.1016/j.apcatb.2023.122806.

## References

[1] L. Wang, R. Lian, Y. Zhang, X. Ma, J. Huang, H. She, C. Liu, Q. Wang, Rational preparation of cocoon-like g-C$_3$N$_4$/COF hybrids: accelerated intramolecular charge delivery for photocatalytic hydrogen evolution, Appl. Catal. B Environ. 315 (2022), 121568.
[2] L. Sun, M. Lu, Z. Yang, Z. Yu, X. Su, Y.Q. Lan, L. Chen, Nickel glyoximate based metal-covalent organic frameworks for efficient photocatalytic hydrogen evolution, Angew. Chem. Int. Ed. 61 (2022), e202204326.
[3] E. Zhao, M. Li, B. Xu, X.L. Wang, Y. Jing, D. Ma, S. Mitchell, J. Perez-Ramirez, Z. Chen, Transfer hydrogenation with a carbon-nitride-supported palladium single-atom photocatalyst and water as a proton source, Angew. Chem. Int. Ed. 61 (2022), e202207410.
[4] S. Zhang, M. Gao, Y. Zhai, J. Wen, J. Yu, T. He, Z. Kang, S. Lu, Which kind of nitrogen chemical states doped carbon dots loaded by g-C$_3$N$_4$ is the best for photocatalytic hydrogen production, J. Colloid Interface Sci. 622 (2022) 662–674.
[5] Y. Wei, L. Chen, H. Chen, L. Cai, G. Tan, Y. Qiu, Q. Xiang, G. Chen, T.C. Lau, M. Robert, Highly efficient photocatalytic reduction of CO$_2$ to CO by in situ formation of a hybrid catalytic system based on molecular iron quaterpyridine covalently linked to carbon nitride, Angew. Chem. Int. Ed. 61 (2022), e202116832.
[6] J. Zhou, J. Li, L. Kan, L. Zhang, Q. Huang, Y. Yan, Y. Chen, J. Liu, S.L. Li, Y.Q. Lan, Linking oxidative and reductive clusters to prepare crystalline porous catalysts for photocatalytic CO$_2$ reduction with H$_2$O, Nat. Commun. 13 (2022) 4681.
[7] Z. Luo, X. Ye, S. Zhang, S. Xue, C. Yang, Y. Hou, W. Xing, R. Yu, J. Sun, Z. Yu, X. Wang, Unveiling the charge transfer dynamics steered by built-in electric fields in BiOBr photocatalysts, Nat. Commun. 13 (2022) 2230.
[8] Y. Li, X.F. Lu, S. Xi, D. Luan, X. Wang, X.W.D. Lou, Synthesis of N-doped highly graphitic carbon urchin-like hollow structures loaded with single-Ni atoms towards efficient CO$_2$ electroreduction, Angew. Chem. Int. Ed. 61 (2022), e202201491.
[9] X. Wang, X. Wang, W. Tian, A. Meng, Z. Li, S. Li, L. Wang, G. Li, High-energy ball-milling constructing P-doped g-C$_3$N$_4$/MoP heterojunction with Mo-N bond bridged interface and Schottky barrier for enhanced photocatalytic H$_2$ evolution, Appl. Catal. B Environ. 303 (2022), 120933.
[10] X. Wang, L. Li, H. Gu, H. Zhang, J. Zhang, Q. Zhang, W.-L. Dai, Highly efficient noble-metal-free NiS/rGO/Cd$_{0.3}$Zn$_{0.7}$S nanorods in visible-light-driven H$_2$ evolution with enhanced surface photoinduced charge transfer, Appl. Surf. Sci. 574 (2022), 151553.
[11] M. Wang, S. Xu, Z. Zhou, C.L. Dong, X. Guo, J.L. Chen, Y.C. Huang, S. Shen, Y. Chen, L. Guo, C. Burda, Atomically dispersed janus nickel sites on red phosphorus for photocatalytic overall water splitting, Angew. Chem. Int. Ed. 61 (2022), e202204711.
[12] Q. Chen, Y. Liu, X. Gu, D. Li, D. Zhang, D. Zhang, H. Huang, B. Mao, Z. Kang, W. Shi, Carbon dots mediated charge sinking effect for boosting hydrogen evolution in Cu-In-Zn-S QDs/MoS$_2$ photocatalysts, Appl. Catal. B Environ. 301 (2022), 120755.
[13] X. Zhang, T. Wu, C. Yu, R. Lu, Ultrafast interlayer charge separation, enhanced visible-light absorption, and tunable overpotential in twisted graphitic carbon nitride bilayers for water splitting, Adv. Mater. 33 (2021), e2104695.
[14] J. Yang, J. Jing, Y. Zhu, A full-spectrum porphyrin-fullerene D-A supramolecular photocatalyst with giant built-in electric field for efficient hydrogen production, Adv. Mater. (2021), e2101026.
[15] J. Kroger, F. Podjaski, G. Savasci, I. Moudrakovski, A. Jimenez-Solano, M. W. Terban, S. Bette, V. Duppel, M. Joos, A. Senocrate, R. Dinnebier, C. Ochsenfeld, B.V. Lotsch, Conductivity mechanism in ionic 2D carbon nitrides: from hydrated ion motion to enhanced photocatalysis, Adv. Mater. 34 (2022), e2107061.
[16] X. Wang, X. Wang, J. Huang, S. Li, A. Meng, Z. Li, Interfacial chemical bond and internal electric field modulated Z-scheme Sv-ZnIn$_2$S$_4$/MoSe$_2$ photocatalyst for efficient hydrogen evolution, Nat. Commun. 12 (2021) 4112.
[17] R. Shen, K. He, A. Zhang, N. Li, Y.H. Ng, P. Zhang, J. Hu, X. Li, In-situ construction of metallic Ni$_3$C@Ni core-shell cocatalysts over g-C$_3$N$_4$ nanosheets for shell-thickness-dependent photocatalytic H$_2$ production, Appl. Catal. B Environ. 291 (2021), 120104.
[18] J. Gao, F. Zhang, H. Xue, L. Zhang, Y. Peng, X. Li, Y. Gao, N. Li, G. Lei, In-situ synthesis of novel ternary CdS/PdAg/g-C$_3$N$_4$ hybrid photocatalyst with

[19] significantly enhanced hydrogen production activity and catalytic mechanism exploration, Appl. Catal. B Environ. 281 (2021), 119509.
[19] H. He, J. Cao, M. Guo, H. Lin, J. Zhang, Y. Chen, S. Chen, Distinctive ternary CdS/Ni$_2$P/g-C$_3$N$_4$ composite for overall water splitting: Ni$_2$P accelerating separation of photocarriers, Appl. Catal. B Environ. 249 (2019) 246–256.
[20] L. Zhang, J. Zhang, H. Yu, J. Yu, Emerging S-scheme photocatalyst, Adv. Mater. (2021), e2107668.
[21] Z. Zhu, Z. Huang, L. Liu, F. Chen, N. Tian, Y. Zhang, H. Yu, Chemically bonded alpha-Fe$_2$O$_3$/Bi$_4$MO$_8$Cl dot-on-plate Z-scheme junction with strong internal electric field for selective photo-oxidation of aromatic alcohols, Angew. Chem. Int. Ed. 61 (2022), e202203519.
[22] Y. Zhai, B. Zhang, R. Shi, S. Zhang, Y. Liu, B. Wang, K. Zhang, G.I.N. Waterhouse, T. Zhang, S. Lu, Carbon dots as new building blocks for electrochemical energy storage and electrocatalysis, Adv. Energy Mater. 12 (2022), 2103426.
[23] J. Liu, Y. Geng, D. Li, H. Yao, Z. Huo, Y. Li, K. Zhang, S. Zhu, H. Wei, W. Xu, J. Jiang, B. Yang, Deep red emissive carbonized polymer dots with unprecedented narrow full width at half maximum, Adv. Mater. 32 (2020), e1906641.
[24] S. Zhu, Q. Meng, L. Wang, J. Zhang, Y. Song, H. Jin, K. Zhang, H. Sun, H. Wang, B. Yang, Highly photoluminescent carbon dots for multicolor patterning, sensors, and bioimaging, Angew. Chem. Int. Ed. 52 (2013) 3953–3957.
[25] T. Zhou, S. Chen, L. Li, J. Wang, Y. Zhang, J. Li, J. Bai, L. Xia, Q. Xu, M. Rahim, B. Zhou, Carbon quantum dots modified anatase/rutile TiO$_2$ photoanode with dramatically enhanced photoelectrochemical performance, Appl. Catal. B Environ. 269 (2020), 118776.
[26] T. Zhou, L. Li, J. Li, J. Wang, J. Bai, L. Xia, Q. Xu, B. Zhou, Electrochemically reduced TiO$_2$ photoanode coupled with oxygen vacancy-rich carbon quantum dots for synergistically improving photoelectrochemical performance, Chem. Eng. J. 425 (2021), 131770.
[27] W. Hui, Y. Yang, Q. Xu, H. Gu, S. Feng, Z. Su, M. Zhang, J. Wang, X. Li, J. Fang, F. Xia, Y. Xia, Y. Chen, X. Gao, W. Huang, Red-carbon-quantum-dot-doped SnO$_2$ composite with enhanced electron mobility for efficient and stable perovskite solar cells, Adv. Mater. 32 (2020), e1906374.
[28] M.H. Elsayed, J. Jayakumar, M. Abdellah, T.H. Mansoure, K. Zheng, A.M. Elewa, C.-L. Chang, L.-Y. Ting, W.-C. Lin, H.-H. Yu, W.-H. Wang, C.-C. Chung, H.-H. Chou, Visible-light-driven hydrogen evolution using nitrogen-doped carbon quantum dot-implanted polymer dots as metal-free photocatalysts, Appl. Catal. B Environ. 283 (2021), 119659.
[29] T. Zhou, J. Wang, Y. Zhang, C. Zhou, J. Bai, J. Li, B. Zhou, Oxygen vacancy-abundant carbon quantum dots as superfast hole transport channel for vastly improving surface charge transfer efficiency of BiVO$_4$ photoanode, Chem. Eng. J. 431 (2022), 133414.
[30] F. Li, Y. Liu, B. Mao, L. Li, H. Huang, D. Zhang, W. Dong, Z. Kang, W. Shi, Carbon-dots-mediated highly efficient hole transfer in I-III-VI quantum dots for photocatalytic hydrogen production, Appl. Catal. B Environ. 292 (2021), 120154.
[31] T. Zhou, S. Chen, J. Wang, Y. Zhang, J. Li, J. Bai, B. Zhou, Dramatically enhanced solar-driven water splitting of BiVO$_4$ photoanode via strengthening hole transfer and light harvesting by co-modification of CQDs and ultrathin β-FeOOH layers, Chem. Eng. J. 403 (2021), 126350.
[32] Y. Zhou, H. Qi, J. Wu, H. Huang, Y. Liu, Z. Kang, Amino modified carbon dots with electron sink effect increase interface charge transfer rate of Cu-based electrocatalyst to enhance the CO$_2$ conversion selectivity to C$_2$H$_4$, Adv. Funct. Mater. (2022), 2113335.
[33] C. Xia, Y. Qiu, Y. Xia, P. Zhu, G. King, X. Zhang, Z. Wu, J.Y.T. Kim, D.A. Cullen, D. Zheng, P. Li, M. Shakouri, E. Heredia, P. Cui, H.N. Alshareef, Y. Hu, H. Wang, General synthesis of single-atom catalysts with high metal loading using graphene quantum dots, Nat. Chem. 13 (2021) 887–894.
[34] M. Han, C. Kang, Z. Qu, S. Zhu, B. Yang, Surface molecule induced effective light absorption and charge transfer for H$_2$ production photocatalysis in a carbonized polymer dots-carbon nitride system, Appl. Catal. B Environ. 305 (2022), 121064.
[35] D. Zhao, K. Sun, W.C. Cheong, L. Zheng, C. Zhang, S. Liu, X. Cao, K. Wu, Y. Pan, Z. Zhuang, B. Hu, D. Wang, Q. Peng, C. Chen, Y. Li, Synergistically interactive pyridinic-N-MoP sites: identified active centers for enhanced hydrogen evolution in alkaline solution, Angew. Chem. Int. Ed. 59 (2020) 8982–8990.
[36] H. Han, J.W. Paik, M. Ham, K.M. Kim, J.K. Park, Y.K. Jeong, Atomic layer deposition-assisted fabrication of Co-nanoparticle/N-doped carbon nanotube hybrids as efficient electrocatalysts for the oxygen evolution reaction, Small 16 (2020), e2002427.
[37] S. Tao, S. Zhu, T. Feng, C. Zheng, B. Yang, Crosslink-enhanced emission effect on luminescence in polymers: advances and perspectives, Angew. Chem. Int. Ed. 59 (2020) 9826–9840.
[38] S. Tao, C. Zhou, C. Kang, S. Zhu, T. Feng, S.T. Zhang, Z. Ding, C. Zheng, C. Xia, B. Yang, Confined-domain crosslink-enhanced emission effect in carbonized polymer dots, Light Sci. Appl. 11 (2022) 56.
[39] Q. Fu, J. Han, X. Wang, P. Xu, T. Yao, J. Zhong, W. Zhong, S. Liu, T. Gao, Z. Zhang, L. Xu, B. Song, 2D transition metal dichalcogenides: design, modulation, and challenges in electrocatalysis, Adv. Mater. (2020), 1907818.
[40] Y. Xu, R. Wang, J. Wang, J. Li, T. Jiao, Z. Liu, Facile fabrication of molybdenum compounds (Mo$_2$C, MoP and MoS$_2$) nanoclusters supported on N-doped reduced graphene oxide for highly efficient hydrogen evolution reaction over broad pH range, Chem. Eng. J. 417 (2021), 129233.
[41] R. Ge, J. Huo, T. Liao, Y. Liu, M. Zhu, Y. Li, J. Zhang, W. Li, Hierarchical molybdenum phosphide coupled with carbon as a whole pH-range electrocatalyst for hydrogen evolution reaction, Appl. Catal. B Environ. 260 (2020), 118196.
[42] L. Zhou, X. Zhang, M. Cai, N. Cui, G. Chen, G. Zou, New insights into the efficient charge transfer of the modified-TiO$_2$/Ag$_3$PO$_4$ composite for enhanced

photocatalytic destruction of algal cells under visible light, Appl. Catal. B Environ. 302 (2022), 120868.

[43] C. Zhang, C. Xie, Y. Gao, X. Tao, C. Ding, F. Fan, H.L. Jiang, Charge separation by creating band bending in metal-organic frameworks for improved photocatalytic hydrogen evolution, Angew. Chem. Int. Ed. 61 (2022), e202204108.

[44] J. Park, H. Yoon, D.-Y. Lee, S.G. Ji, W. Yang, S.D. Tilley, M.-C. Sung, I.J. Park, J. Tan, H. Lee, J.Y. Kim, D.-W. Kim, J. Moon, Photovoltaic powered solar hydrogen production coupled with waste $SO_2$ valorization enabled by MoP electrocatalysts, Appl. Catal. B Environ. 305 (2022), 121045.

[45] F. Yang, D. Liu, Y. Li, S. Ning, L. Cheng, J. Ye, Solid-state synthesis of ultra-small freestanding amorphous MoP quantum dots for highly efficient photocatalytic $H_2$ production, Chem. Eng. J. 406 (2021), 126838.

[46] P. Wei, X. Li, Z. He, Z. Li, X. Zhang, X. Sun, Q. Li, H. Yang, J. Han, Y. Huang, Electron density modulation of MoP by rare earth metal as highly efficient electrocatalysts for pH-universal hydrogen evolution reaction, Appl. Catal. B Environ. 299 (2021), 120657.

[47] K. Wei, H. Nie, Y. Li, X. Wang, Y. Liu, Y. Zhao, H. Shi, H. Huang, Y. Liu, Z. Kang, Carbon dots with different energy levels regulate the activity of metal-free catalyst for hydrogen peroxide photoproduction, J. Colloid Interface Sci. 616 (2022) 769–780.

[48] R.M. Yadav, Z. Li, T. Zhang, O. Sahin, S. Roy, G. Gao, H. Guo, R. Vajtai, L. Wang, P. M. Ajayan, J. Wu, Amine-functionalized carbon nanodot electrocatalysts converting carbon dioxide to methane, Adv. Mater. (2021), e2105690.

[49] H. Song, Y. Li, L. Shang, Z. Tang, T. Zhang, S. Lu, Designed controllable nitrogen-doped carbon-dots-loaded MoP nanoparticles for boosting hydrogen evolution reaction in alkaline medium, Nano Energy 72 (2020), 104730.

[50] Q. Zeng, T. Feng, S. Tao, S. Zhu, B. Yang, Precursor-dependent structural diversity in luminescent carbonized polymer dots (CPDs): the nomenclature, Light Sci. Appl. 10 (2021) 142.

[51] S. Bu, N. Yao, M.A. Hunter, D.J. Searles, Q. Yuan, Design of two-dimensional carbon-nitride structures by tuning the nitrogen concentration, NPJ Comput. Mater. 6 (2020) 128.

[52] Z. Liu, B. Li, Y. Feng, D. Jia, C. Li, Q. Sun, Y. Zhou, Strong electron coupling of Ru and vacancy-rich carbon dots for synergistically enhanced hydrogen evolution reaction, Small 17 (2021), e2102496.

[53] C. Zhang, D. Qin, Y. Zhou, F. Qin, H. Wang, W. Wang, Y. Yang, G. Zeng, Dual optimization approach to Mo single atom dispersed g-$C_3N_4$ photocatalyst: morphology and defect evolution, Appl. Catal. B Environ. 303 (2022), 120904.

[54] Y. Pan, X. Liu, W. Zhang, B. Shao, Z. Liu, Q. Liang, T. Wu, Q. He, J. Huang, Z. Peng, Y. Liu, C. Zhao, Bifunctional template-mediated synthesis of porous ordered g-$C_3N_4$ decorated with potassium and cyano groups for effective photocatalytic $H_2O_2$ evolution from dual-electron $O_2$ reduction, Chem. Eng. J. 427 (2022), 132032.

[55] K. Wang, L. Jiang, T. Xin, Y. Li, X. Wu, G. Zhang, Single-atom V-N charge-transfer bridge on ultrathin carbon nitride for efficient photocatalytic $H_2$ production and formaldehyde oxidation under visible light, Chem. Eng. J. 429 (2022), 132229.

[56] R.-Y. Liu, L. Ding, G.-D. Yang, J.-Y. Zhang, R. Jiao, H.-Z. Sun, Hollow $Mo_2C$ nanospheres modified B-doped g-$C_3N_4$ for high efficient photocatalysts, J. Phys. D Appl. Phys. 55 (2022), 454001.

[57] X. Jiang, Z. Zhang, M. Sun, W. Liu, J. Huang, H. Xu, Self-assembly of highly-dispersed phosphotungstic acid clusters onto graphitic carbon nitride nanosheets as fascinating molecular-scale Z-scheme heterojunctions for photocatalytic solar-to-fuels conversion, Appl. Catal. B Environ. 281 (2021), 119473.

[58] Y. Geng, D. Chen, N. Li, Q. Xu, H. Li, J. He, J. Lu, Z-Scheme 2D/2D α-$Fe_2O_3$/g-$C_3N_4$ heterojunction for photocatalytic oxidation of nitric oxide, Appl. Catal. B Environ. 280 (2021), 119409.

[59] D. Zhu, Q. Zhou, Nitrogen doped g-$C_3N_4$ with the extremely narrow band gap for excellent photocatalytic activities under visible light, Appl. Catal. B Environ. 281 (2021), 119474.

[60] X. Zhang, J. Yan, L.Y.S. Lee, Highly promoted hydrogen production enabled by interfacial P-N chemical bonds in copper phosphosulfide Z-scheme composite, Appl. Catal. B Environ. 283 (2021), 119624.

[61] J. Zhao, B. Fu, X. Li, Z. Ge, B. Ma, Y. Chen, Construction of the $Ni_2P$/MoP heterostructure as a high-performance cocatalyst for visible-light-driven hydrogen production, ACS Appl. Energy Mater. 3 (2020) 10910–10919.

[62] L. Zhang, S. Jin, N. Tsubaki, MoP@$MoO_3$ S-scheme heterojunction in situ construction with phosphating $MoO_3$ for high-efficient photocatalytic hydrogen production, Nanoscale 13 (2021) 18507–18519.

[63] Y. Shen, Y. Jiang, Z. Yang, J. Dong, W. Yang, Q. An, L. Mai, Electronic structure modulation in $MoO_2$/MoP heterostructure to induce fast electronic/ionic diffusion kinetics for lithium storage, Adv. Sci. 9 (2022), e2104504.

[64] B. Wang, C. Yan, G. Xu, X. Shu, J. Lv, Y. Wu, Highly efficient solar-driven photocatalytic hydrogen evolution with $FeMoS_x$/mpg-$C_3N_4$ heterostructure, Chem. Eng. J. 427 (2022), 131507.

[65] L. Ding, L.-J. Wang, R.-Y. Liu, Y.-F. Li, H.-Z. Sun, Carbon nitride based Schottky junction with a Ni-Mo synergistic interaction for highly efficient photocatalytic hydrogen production, Catal. Sci. Technol. 12 (2022) 6465.

[66] C. Jin, C. Xu, W. Chang, X. Ma, X. Hu, E. Liu, J. Fan, Bimetallic phosphide NiCoP anchored g-$C_3N_4$ nanosheets for efficient photocatalytic $H_2$ evolution, J. Alloy. Compd. 803 (2019) 205–215.

[67] L. Ding, F. Qi, Y. Li, J. Lin, Y. Su, Y. Song, L. Wang, H. Sun, C. Tong, In-situ formation of nanosized 1T-phase $MoS_2$ in B-doped carbon nitride for high efficient visible-light-driven $H_2$ production, J. Colloid Interface Sci. 614 (2022) 92–101.

[68] Y. Liu, Y. Zhao, Q. Wu, X. Wang, H. Nie, Y. Zhou, H. Huang, M. Shao, Y. Liu, Z. Kang, Charge storage of carbon dot enhances photo-production of $H_2$ and $H_2O_2$ over $Ni_2P$/carbon dot catalyst under normal pressure, Chem. Eng. J. 409 (2021), 128184.

[69] L. Wang, G. Zhou, Y. Tian, L. Yan, M. Deng, B. Yang, Z. Kang, H. Sun, Hydroxyl decorated g-$C_3N_4$ nanoparticles with narrowed bandgap for high efficient photocatalyst design, Appl. Catal. B Environ. 244 (2019) 262–271.

[70] L. Wang, G. Jin, Y. Shi, H. Zhang, H. Xie, B. Yang, H. Sun, Co-catalyst-free ZnS-$SnS_2$ porous nanosheets for clean and recyclable photocatalytic $H_2$ generation, J. Alloy. Compd. 753 (2018) 60–67.

[71] L. Wang, H. Zhai, G. Jin, X. Li, C. Dong, H. Zhang, B. Yang, H. Xie, H. Sun, 3D porous ZnO-SnS p-n heterojunction for visible light driven photocatalysis, Phys. Chem. Chem. Phys. 19 (2017) 16576–16585.

[72] J.W. Wang, L.Z. Qiao, H.D. Nie, H.H. Huang, Y. Li, S. Yao, M. Liu, Z.M. Zhang, Z. H. Kang, T.B. Lu, Facile electron delivery from graphene template to ultrathin metal-organic layers for boosting $CO_2$ photoreduction, Nat. Commun. 12 (2021) 813.

[73] W. Jiang, Y. Zhao, X. Zong, H. Nie, L. Niu, L. An, D. Qu, X. Wang, Z. Kang, Z. Sun, Photocatalyst for high-performance $H_2$ production: Ga-doped polymeric carbon nitride, Angew. Chem. Int. Ed. 60 (2021) 6124–6129.

[74] Y. Fu, H.-Y. Yu, C. Jiang, T.-H. Zhang, R. Zhan, X. Li, J.-F. Li, J.-H. Tian, R. Yang, NiCo alloy nanoparticles decorated on N-doped carbon nanofibers as highly active and durable oxygen electrocatalyst, Adv. Funct. Mater. 28 (2018) 1705094.

[75] R. Jiang, Q. Li, X. Zheng, W. Wang, W. Liu, S. Wang, Z. Xu, J. Peng, Metal-organic framework-derived Co@NMPC as efficient electrocatalyst for hydrogen evolution reaction: revealing the synergic effect of pyridinic N-Co, Int J. Hydrog. Energy 47 (2022) 27374–27382.

[76] J. Mahmood, F. Li, S.M. Jung, M.S. Okyay, I. Ahmad, S.J. Kim, N. Park, H.Y. Jeong, J.B. Baek, An efficient and pH-universal ruthenium-based catalyst for the hydrogen evolution reaction, Nat. Nanotechnol. 12 (2017) 441–446.

[77] M. Liang, M. Liu, J. Zhang, F. Wang, Z. Miao, L. Diao, J. Mu, J. Zhou, S. Zhuo, Understanding the role of metal and N species in M@NC catalysts for electrochemical $CO_2$ reduction reaction, Appl. Catal. B Environ. 306 (2022), 121115.

[78] J. Chen, J. Huang, Y. Zhao, L. Cao, K. Kajiyoshi, Y. Liu, Z. Li, Y. Feng, Enhancing the electronic metal-support interaction of CoRu alloy and pyridinic N for electrocatalytic pH-universal hydrogen evolution reaction, Chem. Eng. J. 450 (2022), 138026.

[79] S. Yuan, M. Xia, Z. Liu, K. Wang, L. Xiang, G. Huang, J. Zhang, N. Li, Dual synergistic effects between Co and $Mo_2C$ in Co/$Mo_2C$ heterostructure for electrocatalytic overall water splitting, Chem. Eng. J. 430 (2022), 132697.

[80] E. Jiang, J. Li, X. Li, A. Ali, G. Wang, S. Ma, P. Kang Shen, J. Zhu, MoP-$Mo_2C$ quantum dot heterostructures uniformly hosted on a heteroatom-doped 3D porous carbon sheet network as an efficient bifunctional electrocatalyst for overall water splitting, Chem. Eng. J. 431 (2022), 133719.

[81] X. Zhou, Y. Tian, J. Luo, B. Jin, Z. Wu, X. Ning, L. Zhan, X. Fan, T. Zhou, S. Zhang, X. Zhou, MoC quantum dots@N-doped-carbon for low-cost and efficient hydrogen evolution reaction: from electrocatalysis to photocatalysis, Adv. Funct. Mater. 32 (2022), 2201518.

[82] Z. Xu, S. Jin, M.H. Seo, X. Wang, Hierarchical Ni-$Mo_2C$/N-doped carbon Mott-Schottky array for water electrolysis, Appl. Catal. B Environ. 292 (2021), 120168.